

Got Coke? Self-Limiting Poisoning Makes an Ultra Stable and Selective Sub-Nano Cluster Catalyst

Patricia Poths, Guangjing Li, Tsugunosuke Masubuchi, Harry W. T. Morgan, Zisheng Zhang, Anastassia N. Alexandrova,* and Scott L. Anderson*



Cite This: *ACS Catal.* 2023, 13, 1533–1544



Read Online

ACCESS |

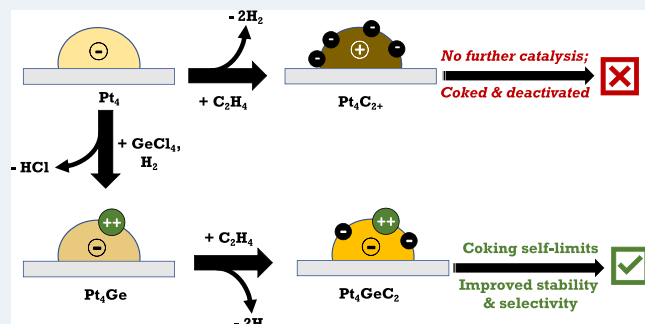
Metrics & More

Article Recommendations

Supporting Information

ABSTRACT: Supported sub-nano clusters hold great promise as economical and highly active catalysts. However, they tend to deactivate rapidly by poisoning and sintering, impeding their widespread use. We find that self-limiting poisoning can stabilize and promote cluster catalysis, that is, poisoning is not always detrimental but can sometimes be exploited. Specifically, Pt–Ge alloy clusters supported on alumina undergo slow and self-limiting coking (carbon deposition) under conditions of thermal dehydrogenation, modifying the cluster framework and electronic properties but preserving the Pt sites required for strong ethylene binding. For the case of Pt₄Ge/alumina, theory shows a number of thermally populated isomers, one of which catalyzes carbon deposition. Because the clusters are fluxional at high temperatures, this isomer acts as a gateway, slowly converting all clusters to Pt₄GeC₂. The surprising result is that Pt₄GeC₂ is highly catalytically active and selective against further coking, that is, coking produces functional, stable catalytic clusters. Ge and C₂ have synergistic electronic effects, leading to efficient and highly selective catalytic dehydrogenation that stops at alkenes and improving stability. Thus, under reaction conditions, the clusters develop into a robust catalyst, suggesting an approach to practicable cluster catalysis.

KEYWORDS: sub-nano clusters, bimetallic catalyst, selective dehydrogenation, carbon poisoning prevention, sintering prevention



INTRODUCTION

There is a great drive to go sub-nano in precious metal catalysis because in sub-nano clusters nearly all expensive metal atoms are exposed to reactants, increasing cost-effectiveness. Clusters can also have better catalytic activity than bulk metal,¹ provide a parameter for catalyst tuning (size), and can break scaling relations that can limit the activity of larger catalytic centers.² Pt-based catalysts are widely used in refining, transforming chemicals, and converting environmentally harmful products,^{3–7} and the challenge of using sub-nano Pt catalysts in such applications relates to stability. Because the metal–metal coordination is low, few-atom clusters are significantly more susceptible than larger nanoparticles to both thermal sintering and poisoning. For example, in alkane dehydrogenation for alkene production, the high operating temperatures can lead to sintering, and reactive sites are easily poisoned by carbon deposition (“coking”) if the catalyst selectivity is not high enough. Past research showed that sintering and coking can be inhibited by growing porous overcoatings on nanometer catalyst particles,⁸ but this approach partially blocks the catalytic sites, limiting efficiency.^{3,9} For sub-nano Pt clusters deposited on SiO₂ supports, we showed that even a single cycle of alumina atomic layer deposition overcoating completely blocked all Pt sites,

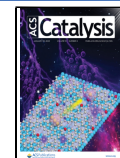
rendering the clusters inert.¹⁰ Coked catalysts are often regenerated by oxidizing away carbon deposits at high temperatures, however, that would tend to deactivate sub-nano clusters by sintering.^{11,12} Alloying sub-nano clusters to modify the chemical and thermal properties is another approach, for example, alloying oxide-supported Pt cluster catalysts with tin or boron prevents carbon deposition and inhibits sintering,^{13–16} however, these elements are not ideal because they also block a substantial fraction of the catalytically active Pt sites.

Germanium was recently suggested by Jimenez-Izal et al.¹⁷ as a dopant for small Pt clusters to inhibit coking and sintering under conditions of alkane dehydrogenation. Supported Pt₂Ge clusters were predicted to be more sinter-resistant than Pt₃, Pt₂Sn, and Pt₂Si clusters and to be highly active for ethane dehydrogenation to ethylene, while being highly selective against deeper dehydrogenation that tends to lead to coking.

Received: November 16, 2022

Revised: December 21, 2022

Published: January 10, 2023



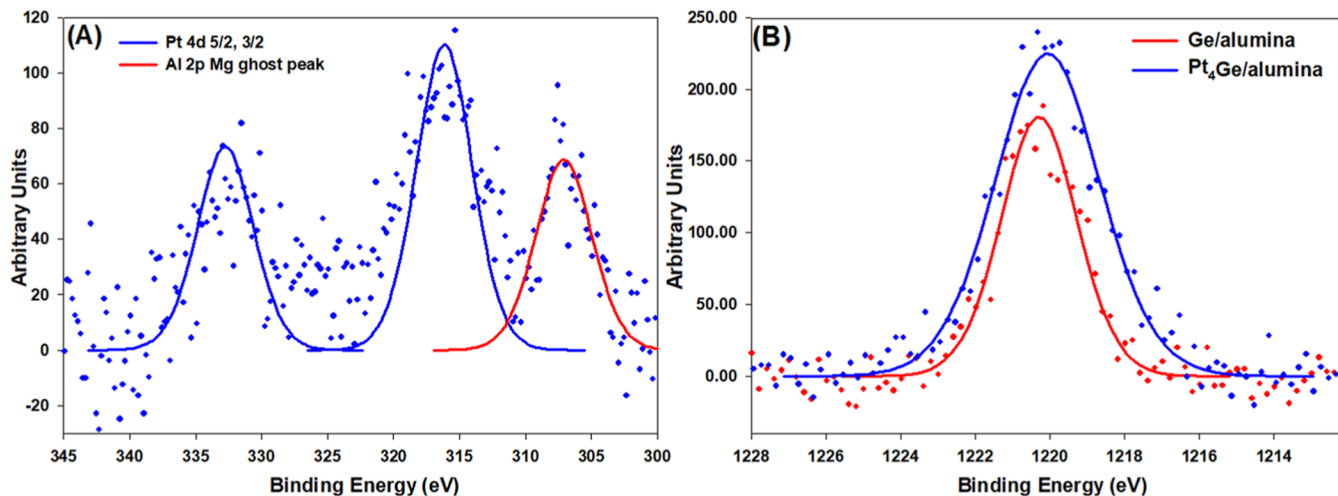


Figure 1. XPS showing selective binding of Ge to Pt clusters. (A) XPS of Pt 4d 5/2 and 3/2 of Pt₄Ge/alumina, red colored peak is from Mg contamination in the Al source. (B) Ge 2p 3/2 peak for Ge/alumina in red and Pt₄Ge/alumina in blue.

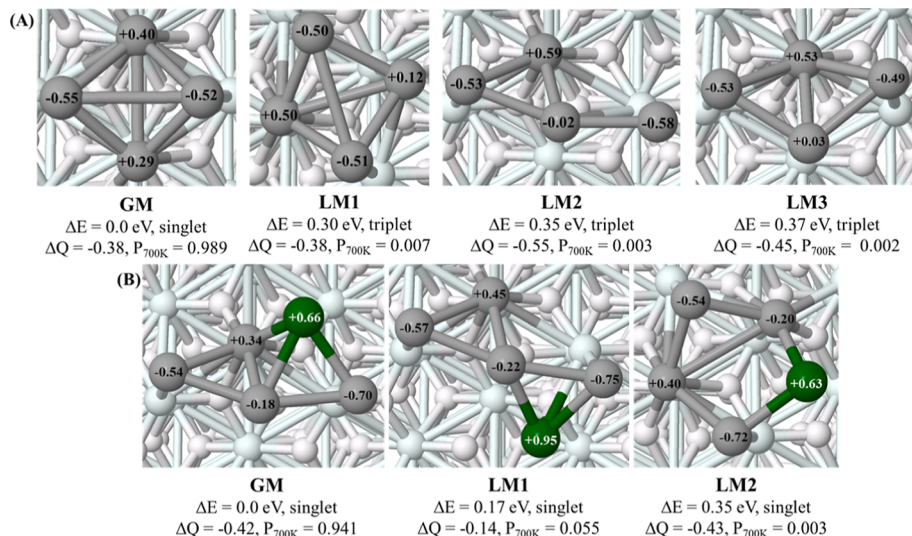


Figure 2. Thermally accessible structures, which are within 0.4 eV of the lowest energy structure. (A) Computed thermally accessible structures of Pt₄/alumina. (B) Computed thermally accessible structures of Pt₄Ge/alumina. The spin state, net support-to-cluster electron transfer (ΔQ), Bader charges on each cluster atom, and the thermal population at 700 K (P_{700K}) are shown. GM = global minimum. For each LM, the energy above the GM (ΔE) is given. Images showing the entire supercell are in the Supporting Information.

Although density functional theory (DFT) simulations were promising, previous experimental work on Ge-containing catalysts was not always successful. For example, several studies found that activity for dehydrogenation of cyclohexane was substantially lower for PtGe catalysts than for analogous Pt catalysts.^{18,19} Note, however, that these studies focused on catalysts with particle sizes much larger than the sub-nano clusters examined here. Here, we report a novel approach to improving cluster catalyst stability, in which *self-limiting* coking converts alumina-supported Pt_nGe_x catalyst clusters to a Pt_nGe_xC_y form that is catalytically active and thermally and chemically stable. The effect is illustrated here using Pt₄Ge and Pt₄GeC₂ catalyst clusters, focusing on two critical factors in the overall process of ethane-to-ethylene dehydrogenation—high selectivity toward desorption of intact ethylene (avoiding deeper dehydrogenation/coking) and maintaining a large number of strong ethylene binding sites required to promote ethane-to-ethylene conversion. The actual ethane-to-ethylene step is assessed by DFT only because ethane sticks too weakly

to study by our ultrahigh vacuum (UHV) surface science methods.

RESULTS AND DISCUSSION

Pt₄Ge/Alumina Characterization. As described in the Methods section, Pt₄Ge/alumina samples were prepared by soft-landing mass-selected Pt₄ clusters on thin-film alumina supports, followed by Ge addition by exposure to GeCl₄ and H₂. The Pt₄ cluster coverage was 3.8×10^{13} clusters/cm², equivalent to 10% of a close-packed Pt monolayer (ML). S/TEM imaging on both carbon and alumina-coated aluminum grids is described in the Supporting Information (Figure S1). Individual atoms were not resolved, but from the cluster spot densities, sizes, and stability under the e-beam, we conclude that small Pt_n is stable at room temperature on both carbon and alumina. One question is whether the Pt clusters remain adsorbed at their landing sites, or if they might diffuse and bind at defects in the alumina film. Evidence bearing on this question is discussed in the Supporting Information, leading to

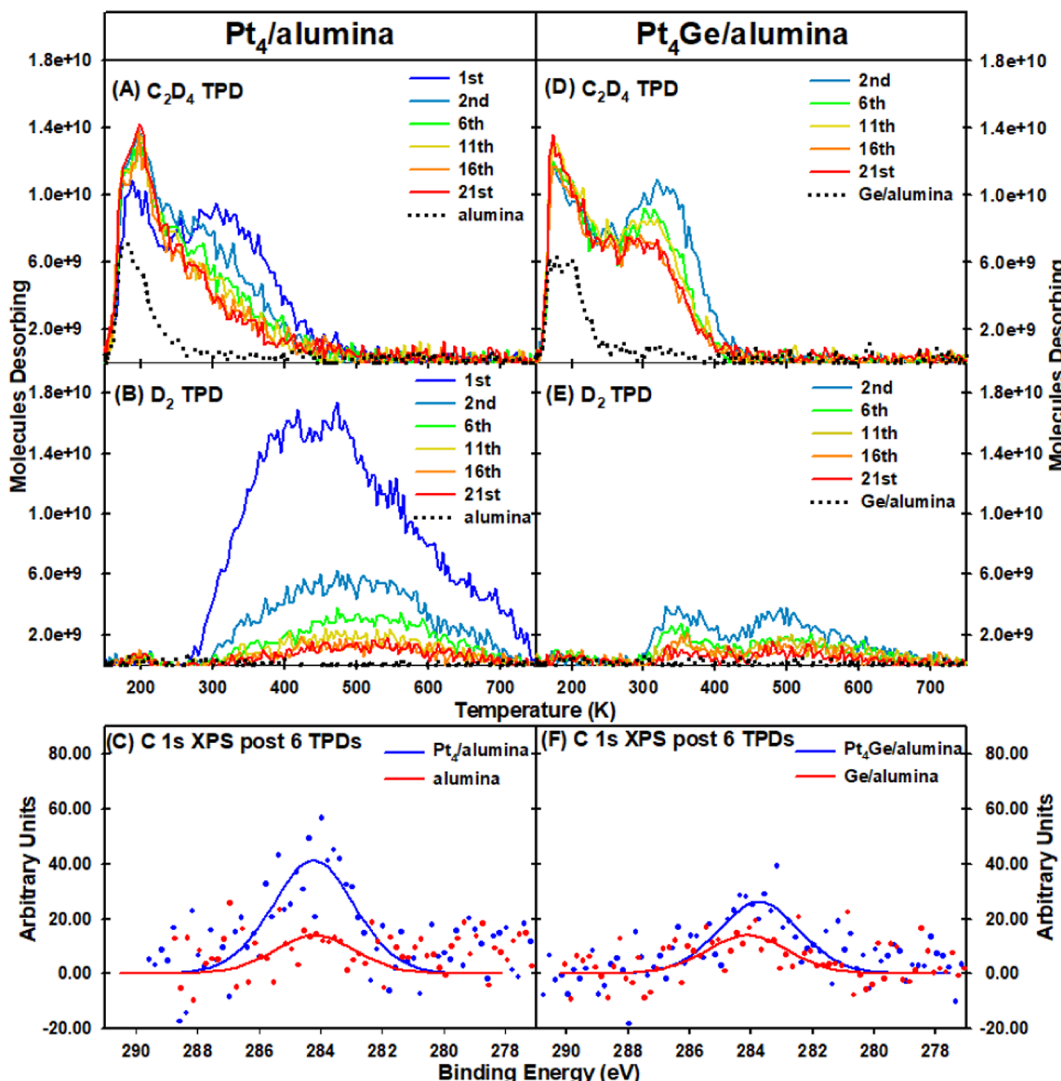


Figure 3. Temperature-programmed desorption (TPD) results showing C₂D₄ and D₂ desorption, with XPS scans of the C 1s region. Left column: Pt₄/alumina. Right column: Pt₄Ge/alumina. (A,D) show desorption of intact C₂D₄. (B,E) show desorption of D₂. (C,F) show carbon 1s XPS from Pt₄/alumina and Pt₄Ge/alumina after six TPD cycles; control samples (alumina and Ge/alumina) were also probed post the six TPDs.

the conclusion that the Pt clusters do not diffuse to and bind at defects, apart from a small fraction that probably landed on or close to such sites.

X-ray photoelectron spectroscopy (XPS) images were used to measure the Ge/Pt stoichiometry, using an approach discussed in the *Supporting Information*. The resulting Ge/Pt ratio was found to be 1.07:4, that is, one Ge atom was deposited *per* Pt₄ cluster. In addition, there was some non-specific Ge deposition on the alumina support, but as shown below and in the *Supporting Information*, this alumina-bound Ge is not catalytically active itself and has little effect on the catalytic properties of Pt_n clusters deposited on a Ge-treated alumina support. Note that the XP spectra shown in Figure 1 were taken for the as-prepared samples (after H₂ exposure that removed most but not all of the Cl atoms from the GeCl₄ precursor). These Cl atoms complicate interpretation of the Pt and Ge binding energies.

Cluster Structures from DFT. Figure 2 shows the thermally accessible isomers for Pt₄/ α -Al₂O₃ (Figure 2A) and Pt₄Ge/ α -Al₂O₃ (Figure 2B), calculated using global optimization at the DFT level, as described in the *Methods* section. The predicted isomer populations at 700 K, near the

upper end of the experimental temperature range, are given as P_{700K} . For Pt₄/alumina, the global minimum (GM) structure is a spin-singlet, but all other thermally accessible local minima (LMs) are spin-triplets. The structures have Pt atoms with both positive and negative charges, but in all cases, there is net support-to-cluster electron transfer (ΔQ). For Pt₄Ge/alumina, the GM and all thermally accessible LMs are singlets, with substantial Ge-to-Pt₄ electron transfer and also net support-to-cluster electron transfer.

Ethylene Temperature-Programmed Desorption Analysis. For selective alkane dehydrogenation, it is critical that the nascent alkene product desorbs from the catalyst, rather than undergoing further dehydrogenation or decomposition that tends to deposit carbon. In addition, the catalyst clusters must provide large numbers of strong alkene binding sites to enhance alkane-to-alkene conversion. To probe the branching between alkene desorption versus unwanted dehydrogenation/coking, we have adopted the strategy of adsorbing ethylene on the catalyst at low temperature, then measuring, using temperature-programmed desorption (TPD), the branching between intact ethylene desorption versus hydrogen desorption, which signals dehydrogenation and

carbon deposition. In addition, C 1s XPS after multiple ethylene adsorption/desorption cycles was used to directly measure the tendency toward carbon deposition.

Figure 3 shows TPD data collected for Pt₄/alumina and Pt₄Ge/alumina samples, both with identical, 0.1 ML equivalent of Pt deposited as Pt₄ clusters. The data shown are from experiments in which 21 sequential TPD runs were done for each sample. For each run, the sample was first exposed to a saturation dose of C₂D₄ (10 L) at 150 K and then heated at 3 K/s to 750 K while mass-spectrometrically monitoring desorption of C₂D₄ and D₂. No signal was observed for desorption of acetylene or other hydrocarbon species, and no additional D₂ desorbed in test experiments in which the samples were ramped to higher temperatures, indicating that ethylene either desorbed intact or dehydrogenated to 2 C_(ads) + 2 D_(gas).

For comparison, the figure also shows the desorption signals observed from the alumina and Ge-treated alumina (Ge/alumina) supports with no clusters present. For both supports, C₂D₄ corresponds to a few percent of a ML adsorbed during the 150 K dose, desorbing below 250 K when heated. This support-bound C₂D₄ is attributed to binding at defects in the alumina film. No D₂ desorption was observed, showing that neither the alumina nor Ge/alumina supports were active for ethylene dehydrogenation, and as might be expected, the desorption signals in repeated runs were unchanged.

During the first TPD from the Pt₄/alumina sample, there was substantial C₂D₄ desorption in the 250–450 K range, corresponding to ethylene binding to the Pt₄ clusters, in addition to a lower temperature feature attributed primarily to weak binding to the alumina support. D₂ desorbed in a broad feature extending from 250 to 750 K, implying that many of the C₂D₄ molecules dehydrogenated, liberating D₂ and depositing carbon. During the second run, there was substantially less C₂D₄ desorption above 250 K and a general shift to desorption at lower temperatures, implying fewer and weaker C₂D₄ binding sites. The amount of D₂ desorption also decreased, suggesting that dehydrogenation occurs primarily for strongly bound C₂D₄, but that the number of such sites was much smaller in the second TPD cycle due to coking and/or sintering. As additional cycles were carried out, the decrease in C₂D₄ desorption at high temperatures, and the reduction in D₂ desorption continued, with the rate of change slowing as the clusters were mostly deactivated.

The 21 TPD run experiments took >20 h each, making repetition impractical and raising the possibility that surface contamination might have influenced the results in later cycles. Therefore, we also carried out repeated experiments studying the effects of the first six TPD runs, which were responsible for most of the change in catalyst properties. Quantitative analysis of the desorption is based on these six TPD experiments. As described elsewhere,¹³ it is possible to calibrate the absolute sensitivity of the TPD system, and Table S1 gives the numbers of C₂D₄ and D₂ molecules desorbing per Pt₄ cluster in each of the six TPD runs, averaged over the four available data sets. Because there was no evidence of adsorbed hydrogen remaining at 750 K, the number of C atoms deposited should be equal to the number of D₂ molecules desorbing, and the total number of C₂D₄ molecules adsorbed during each 150 K dose can be estimated as the number of C₂D₄ desorbing + half the number of D₂ desorbing. During the first TPD, an average of ~2.9 C₂D₄/Pt₄ were adsorbed, of which ~56% desorbed intact, with the remainder dehydrogenating to liberate D₂ and

deposited an average of ~2.5 C atoms/cluster. Because of the cluster isomer distribution, some cluster-to-cluster variation is expected, but we interpret the first TPD desorption numbers as indicating that three C₂D₄ molecules typically adsorbed per cluster at 150 K, of which two typically desorbed intact upon heating, the other decomposing to liberate 2 D_{2(gas)} and deposit 2 C per cluster. By the sixth TPD cycle, the number of C₂D₄ adsorbed per Pt₄ had dropped ~58% to just ~1.23, of which ~82% desorbed intact, with the remainder decomposing to deposit C and liberate D₂. For the Pt₄/alumina sample, the total D₂ desorption during the six TPD runs corresponded to the deposition of ~5.75 C atoms per deposited Pt₄ cluster.

Pt₄Ge/alumina presents a striking contrast. As described in the Methods, the final step in Pt₄Ge/alumina preparation involved 750 K heating to desorb residual Cl and hydrogen (as HCl and H₂—Figure S2) and to emphasize the point that the Pt₄Ge/alumina samples had already been heated once prior to the initial C₂D₄ TPD runs; the TPD cycles in Figure 3D,E are numbered starting with “2nd TPD”. The C₂D₄ desorption observed in this second TPD for Pt₄Ge/alumina was quite similar in both intensity and structure to that in the first run on Pt₄/alumina, with a low-temperature component at least partly due to desorption from the Ge/alumina substrate, and a high-temperature component attributed to sites on the Pt₄Ge clusters. In contrast, D₂ desorption (i.e., carbon deposition) was much weaker for Pt₄Ge than in either the first or second TPD runs for Pt₄/alumina and had a bi-modal temperature dependence, suggesting that what little D₂ desorbed was produced by two processes with different activation energies. The D₂ desorption features can, in principle, be fit to extract E_a values, requiring some assumption about the kinetic order of the rate-limiting steps. We previously examined D₂ TPD from small Pt_n/alumina exposed to D₂ under conditions similar to those used here for C₂D₄,²⁰ observing recombinative desorption starting at ~230 K, peaking just below 300 K, and terminating at ~450 K. The fact that the desorption features for D₂ generated by C₂D₄ decomposition do not match the recombinative feature observed in D₂ TPD suggests that some other step in the D₂ production pathway is rate limiting. For simplicity, we assume that this step follows first-order kinetics²¹ and further assume a prefactor of 10¹⁵ s⁻¹. This crude approximation gives effective (i.e., averaged over all accessible pathways and cluster isomers) E_a values of ~1.1 V for the 350 K feature and ~2.5 eV for the 500 K feature, in the range observed for C–H activation in the DFT calculations. During subsequent TPD cycles, there continued to be a small and diminishing amount of D₂ production, and the C₂D₄ desorption behavior evolved but note that when a steady state had been reached after ~15 runs, the C₂D₄ desorption, particularly at higher temperatures, was substantially higher for Pt₄Ge than for Pt₄.

Again, quantitative desorption analysis was done for the first six TPD runs. The total number of C₂D₄ molecules adsorbed per Pt₄Ge cluster in the second TPD was ~1.71, of which ~86% desorbed intact, with the balance decomposing to liberate D₂ and deposit ~0.5 C/cluster on average (Table S2). Given that C atoms deposit in pairs (no desorption of C₁ or C_{>2} species is observed), we interpret this to mean that the Pt₄Ge clusters initially had one or two C₂D₄ molecules adsorbed and that on ~25% of the clusters, one ethylene decomposed to deposit two C atoms. Thus, the probability of carbon deposition during this first TPD run was ~one-fourth that for the Pt₄/alumina samples. By the sixth TPD cycle, the

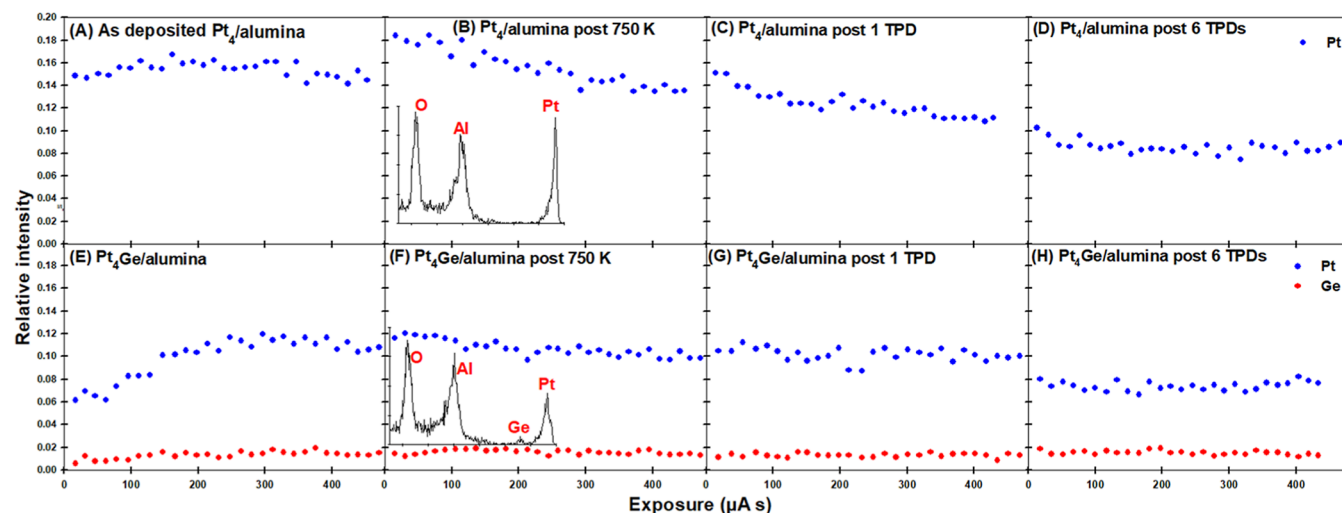


Figure 4. Low-energy He^+ ISS showing relative intensities of Pt and Ge. (A) As-deposited $\text{Pt}_4/\text{alumina}$, (B) $\text{Pt}_4/\text{alumina}$ post 750 K heat, inset shows the raw ISS at $\sim 30 \mu\text{As}$ exposure. (C) $\text{Pt}_4/\text{alumina}$ post one C_2D_4 TPD, (D) $\text{Pt}_4/\text{alumina}$ post six C_2D_4 TPDs, (E) As-prepared $\text{Pt}_4\text{Ge}/\text{alumina}$, (F) $\text{Pt}_4\text{Ge}/\text{alumina}$ post 750 K heat, inset shows the raw ISS at $\sim 30 \mu\text{As}$ exposure. (G) $\text{Pt}_4\text{Ge}/\text{alumina}$ post one C_2D_4 TPD, and (H) $\text{Pt}_4\text{Ge}/\text{alumina}$ post six C_2D_4 TPDs.

number of adsorbing C_2D_4 molecules was still $\sim 1.46/\text{cluster}$, of which 91% desorbed intact, with the balance decomposing to liberate D_2 and deposit just $\sim 0.28 \text{ C/Pt}_4\text{Ge}$ cluster. Thus, during the second TPD for $\text{Pt}_4\text{Ge}/\text{alumina}$, the number of ethylene adsorbing *per* cluster was $\sim 41\%$ lower than in the first TPD for $\text{Pt}_4/\text{alumina}$, but by the sixth TPD, the number was $\sim 20\%$ higher for Pt_4Ge . We interpret this to imply that addition of a Ge atom reduced the initial number of ethylene binding sites, but the binding sites, particularly the catalytically important strong/high temperature binding sites, survived much better under reaction conditions for Pt_4Ge than for Pt_4 .

From the total D_2 desorption during the six TPD runs, we estimate that the total carbon deposition on $\text{Pt}_4\text{Ge}/\text{alumina}$ amounts to $\sim 1.8 \text{ C atoms per}$ deposited Pt_4Ge cluster, which is less than a third of the total estimated for $\text{Pt}_4/\text{alumina}$ ($5.75 \text{ C}/\text{cluster}$). It should be noted that due to uncertainties in the intensity calibration process, the absolute desorption numbers given here and in Tables S1 and S2 are uncertain by $\sim 50\%$; however, the relative uncertainties for comparing TPD data in different experiments are smaller—on the order of $\pm 10\%$. Thus, the TPD data indicate that $\text{Pt}_4/\text{alumina}$ cokes more than a factor of 3 faster than $\text{Pt}_4\text{Ge}/\text{alumina}$.

Carbon Deposition Analysis. Carbon deposition was also probed directly by C 1s XPS after the six TPDs, as summarized in Figure 3C,F. XPS spectra are shown for the $\text{Pt}_4/\text{alumina}$ and $\text{Pt}_4\text{Ge}/\text{alumina}$ samples and for Pt-free alumina and Ge/alumina samples after the six C_2D_4 TPDs. The signals are weak because the coverage of clusters, responsible for most carbon deposition, was small, as is the C 1s photoemission cross section. Nonetheless, it is clear that the C 1s signal for $\text{Pt}_4/\text{alumina}$ is substantially larger than the signal for the alumina support, and after subtracting the support contribution, the net carbon deposition corresponds to $\sim 8 \pm 5 \text{ C atoms}/\text{cluster}$. The C/Pt ratio was calculated assuming that both C and Pt are in the surface layer, in which case $\text{C/Pt} = (I_{\text{C}} \cdot \sigma_{\text{Pt}}) / (I_{\text{Pt}} \cdot \sigma_{\text{C}})$, where I_{C} and I_{Pt} are the integrated intensities for the C 1s and Pt 4d peaks, and σ_{C} and σ_{Pt} are the sublevel photoemission cross sections.²² The C 1s signal for the $\text{Pt}_4\text{Ge}/\text{alumina}$ sample is smaller, and after subtracting the support contribution, the carbon deposition is estimated to be $3 \pm 3 \text{ C atoms/Pt}_4\text{Ge}$

cluster. Thus, both the absolute number of deposited C atoms/cluster, and the $\sim 3:1$ ratio of C deposition on Pt_4 compared to Pt_4Ge , are consistent with the values derived from the analysis of D_2 TPD.

To provide additional insight into the carbon/Pt morphology, the samples were also probed by low-energy He^+ ion scattering before and after six TPDs (Figure 4). Example ion-scattering spectroscopy (ISS) spectra shown as insets have peaks due to He^+ scattering from individual Pt, Ge, Al, and O atoms in the top-most sample layer, superimposed on a smooth background from multiple or sub-surface scattering processes. The background rises sharply at lower energies, preventing direct observation of surface carbon. The main plots in Figure 4 show how the background-subtracted Pt and Ge peak intensities vary as a function of exposure to the $\sim 0.35 \mu\text{A}$ He^+ beam, which slowly sputters materials from the surface. To compensate for any He^+ intensity variations, the Pt and Ge intensities are normalized to the total (Pt + Ge + Al + O) intensity, which is nearly invariant under He^+ exposure.

For the as-deposited $\text{Pt}_4/\text{alumina}$ (Figure 4A), the Pt ISS intensity initially increased slightly, then slowly declined at long exposures as Pt atoms were slowly sputtered from the surface. The slight increase was attributed to the exposure of additional Pt due to sputter removal of a small coverage of adventitious adsorbates, for example, H_2 or CO, which have partial pressures $\leq 5 \times 10^{-11}$ Torr in the UHV system. If an as-deposited $\text{Pt}_4/\text{alumina}$ sample is briefly heated to 750 K to remove the adsorbates prior to ISS analysis (Figure 4B), the Pt intensity is higher than in the unheated sample and simply decreases with exposure time as Pt is sputtered. Note that if the Pt_4 clusters had sintered at 750 K to form larger, multilayer clusters on the surface, this would have substantially decreased the Pt ISS intensity, thus such extensive sintering is ruled out by the result in Figure 4B, consistent with the conclusions from the S/TEM data. The initial Pt ISS intensity for $\text{Pt}_4/\text{alumina}$ after a single C_2D_4 TPD experiment (Figure 4C) was $\sim 18\%$ smaller than that for the 750 K heated $\text{Pt}_4/\text{alumina}$ sample in Figure 4B, suggesting that the Pt signal was attenuated by deposited carbon, and the attenuation increased after six TPDs (Figure 4D), as expected.

The as-prepared Pt₄Ge/alumina sample was probed both before (Figure 4E) and after (Figure 4F) the 750 K heating used to remove residual H and Cl from clusters. For the unheated clusters, the initial Pt and Ge intensities were small, increasing as the adsorbed H and Cl were sputtered, exposing underlying Pt and Ge atoms. Both Pt and Ge signals decreased slightly at long exposures as Pt and Ge were lost to sputtering. For the sample probed after 750 K heating (Figure 4F), the initial Pt and Ge intensities were similar to the maximum intensities seen for the unheated sample, that is, removing the adsorbates by heating versus He⁺ sputtering had similar effects. The initial Pt ISS signal for the heated Pt₄Ge/alumina sample was ~37% smaller than the signal observed for heated Pt₄/alumina, presumably reflecting some shadowing or blocking of He⁺ scattering from Pt by the Ge atom. The 37% lower Pt ISS intensity was quite similar to the 41% lower total adsorbed C₂D₄ measured in the initial Pt₄Ge/alumina TPD (Tables S1 and S2). For Pt₄Ge/alumina samples that were heated to 750 K and then subjected to either one or six TPD runs (Figure 4G,H), the Pt intensities were attenuated compared to the heated sample, as expected from the fact that some carbon deposition occurred.

The post-six-TPD initial Pt ISS intensity for the Pt₄/alumina sample (Figure 4D) was ~44% attenuated compared to the initial intensity of the 750 K heated Pt₄/alumina sample. It is not surprising that there was attenuation, given the carbon deposition observed by TPD and XPS (~6 C/cluster from TPD, ~8 C/cluster from XPS). Indeed, the surprise is that the attenuation was not much larger. For example, 5- and 20-fold attenuations of the Pt ISS signals were found to result from adsorption of just a single layer of H or O atoms, respectively, on sub-nano Pt_n/SiO₂.²³ Thus, the much smaller Pt ISS attenuation indicates that the C atoms must primarily be bound in sites where they have little effect on He⁺ scattering from Pt, such as sites around the cluster periphery or buried in the cluster core. Nonetheless, the TPD results show that these C atoms strongly attenuate strong ethylene binding, suggesting that carbon has a substantial electronic effect.

For the Pt₄Ge/alumina sample after six TPDs (Figure 4H), the initial Pt signal was ~31% attenuated, relative to the heated Pt₄Ge/alumina (Figure 4F), which can be compared to the amount of C deposition seen from TPD (~1.8/cluster) and XPS (~3/cluster). For both Pt₄ and Pt₄Ge samples, ISS indicates that a significant fraction of the Pt atoms remained accessible to He⁺ scattering after six TPD runs.

To summarize the experiments, adding a single Ge atom reduced carbon deposition by a factor of ~3, but there was still significant carbon deposition for Pt₄Ge, amounting to ~2 C atoms/cluster after six TPD runs. Nonetheless, the Pt₄Ge clusters retained most of their strong/high-temperature ethylene binding sites, even after 21 TPD runs, while these high-temperature sites were almost entirely suppressed for Pt₄/alumina. Questions we seek to address are: Why is carbon deposition only partly suppressed for Pt₄Ge/alumina? What is the nature of the strong (high-temperature) ethylene binding sites retained for Pt₄Ge but lost for Pt₄/alumina? And why, despite retaining strong C₂D₄ binding sites, does Pt₄Ge nearly stop producing D₂?

DFT was used to address these questions and to examine the activity of the model catalysts for the ethane-to-ethylene dehydrogenation reaction, which cannot be studied under surface science conditions.

DFT of Ethane, Ethylene, and Acetylene C–H Activation Barriers. Pt₄Ge/alumina clusters are found to strongly bind and activate ethane on all thermally accessible isomers (Figure 2B), and there are well over 50 configurations for C₂H₆–Pt₄Ge/alumina with energies below 0.4 eV, that is, with non-zero thermal populations at 700 K. All of the low-lying configurations appear to activate ethane, as shown by C–H bond elongations ranging from 1.140 to 1.158 Å, compared to the un-activated C–H bond length of 1.09 Å. Figure 5A illustrates two reactant configurations and gives energies (horizontal lines) for a dozen more. The two illustrated are built on the GM and on the second local minimum (LM2) for the bare Pt₄Ge cluster. The LM2-based structures are singled out for reasons that will be made clear shortly. Once

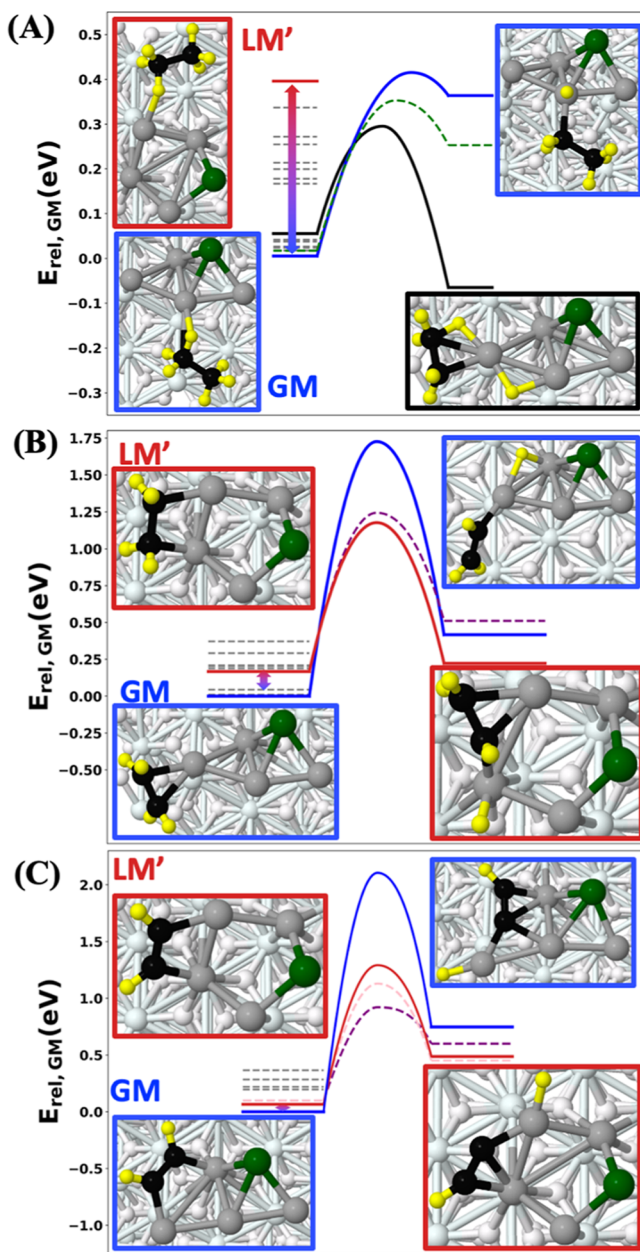


Figure 5. Representative ethane, ethylene, and acetylene C–H activation barriers for Pt₄Ge. C–H activation barriers on Pt₄Ge/alumina thermal ensemble of states for (A) ethane, (B) ethylene, and (C) acetylene.

adsorbates bind to LM2, the structures are labeled LM' because their thermal accessibility is changed by the binding of adsorbates. For all lowest-energy configurations, the activation barriers for breaking the first C–H bond are found to be ≤ 0.4 eV, well below the energy for desorption of ethane from the clusters (≤ 0.6 eV, see Figure S4 and text). Thus, DFT shows that ethane should bind to all isomers of Pt₄Ge/alumina and dehydrogenate in preference to desorbing. Another factor that tends to promote dehydrogenation is that the H atom products readily recombine and desorb as H₂ at moderate temperatures, as shown in Figure 3E. To verify that Pt₄Ge clusters are not poisoned by ethyl, we computed the activation barrier activating the second C–H bond, for the initial low-barrier pathway. This second C–H activation barrier is practically negligible (0.02 eV), and the resulting structure for ethylene + 2H bound to Pt₄Ge was ~ 0.74 eV lower in energy than the ethyl-bound intermediate (Figure S6), which was already ~ 0.1 eV below intact ethane bound to the cluster. Therefore, we conclude that Pt₄Ge should be highly active for ethane dehydrogenation to ethylene + 2H.

To examine the pathways that must ultimately lead to carbon deposition, we next performed DFT calculations for ethylene and acetylene binding and dehydrogenation on the thermally accessible isomers of the Pt₄Ge clusters (Figure 5B,C). Note that adsorbates can bind with different energies on different cluster isomers, which can significantly change isomer populations, with important effects on the mechanism. We found that ethylene predominantly binds to the Pt₄Ge clusters (including the most abundant GM) in the π -mode, that is, with the ethylene π bond coordinated to a single Pt atom, retaining the C sp²-hybridization (Figure S7). The barriers for the GM π -mode-bound ethylene to undergo C–H dissociation are higher than the desorption energies, and thus π -mode-bound ethylene is predicted to mostly desorb intact, rather than undergoing further dehydrogenation, consistent with the small D₂ desorption branching observed for the Pt₄Ge/alumina catalyst. Importantly, however, one of the thermally accessible isomers of ethylene–Pt₄Ge, LM' (corresponding to LM2 of the bare cluster), binds ethylene in a di- σ mode (Figure 5B), and in this configuration the barrier to C–H dissociation is significantly lower than in any of the π -mode-bound configurations. Furthermore, the LM' isomer binds ethylene much more strongly than the GM isomer, with an adsorption energy of -1.96 eV (Figures S7 and S8). LM2 for the bare cluster has P_{700K} of only 0.3%—far too small to account for the amount of D₂ desorption observed during TPD. However, the ethylene di- σ bond in LM' is strong, stabilizing LM' and increasing its P_{700K} to $\sim 3\%$.

We propose that dehydrogenation on an isomer with small, but significant population, accounts for carbon deposition being only partly suppressed for Pt₄Ge/alumina. Specifically, during each TPD cycle, most of the Pt₄Ge would desorb C₂D₄ intact, but the small fraction in LM' configurations would dehydrogenate C₂D₄, giving rise to the observed small D₂ signals. Isomerization between the thermally accessible isomers within the ensemble ensures that LM' is repopulated in each TPD cycle, and thus LM' acts as a “gateway” isomer that keeps dehydrogenating ethylene on a fraction of the cluster population during repeated TPD cycling. We expect that all of the clusters eventually pass through this gateway during repeated TPD cycling, becoming coked. The calculated population of the C₂D₄-LM' isomer ($\sim 3\%$) is smaller than the population ($\sim 25\%$) suggested by D₂ TPD signal; however,

we note that isomer populations depend exponentially on their relative energies, thus amplifying the effects of small DFT errors.

For coke to form, dehydrogenation must proceed further, beyond acetylene. With acetylene bound to Pt₄Ge (Figures 5C, S9), the isomer populations adjust again: the LM' isomer drops even further in energy relative to the GM, such that its P_{700K} increases to $\sim 10\%$ of the total population. The population dehydrogenates acetylene with a high propensity, rather than desorbing it, as suggested by the fact that in a number of the low-lying isomers of C₂H₂–Pt₄Ge/alumina, acetylene dehydrogenates spontaneously (Figure S9). For the thermally accessible isomers in which C₂H₂ remains intact, the computed first C–H dissociation barriers are well below the desorption energies for intact acetylene, which exceed 2 eV from all isomers (Figures 5C, S10). Notably, LM'-based isomers continue to dehydrogenate more aggressively than GM-based isomers, judging by the computed barriers, and new Pt₄Ge core isomers are stabilized due to the strong binding of acetylene, providing lower-barrier routes for dehydrogenation (Figure 5C, dashed lines, Figure S10 for structures). Hence, theory predicts that once acetylene forms on the Pt₄Ge cluster, regardless of the isomer, it will always dehydrogenate, though higher-energy isomers will dehydrogenate at lower temperatures, some with dehydrogenation barriers less than 1 eV. This prediction is consistent with the observation that no intact acetylene desorption is ever seen for Pt₄Ge/alumina in the experiments (Figure S11). Thus, in ethylene TPD (and in the ethane-to-ethylene reaction), we predict that Ge addition largely, but not completely, suppresses carbon deposition, such that in repeated TPD cycles (or long reaction times) the clusters will slowly all become coked by at least a pair of carbon atoms, with the LM' isomer serving as a gateway to coking.

To assess the favorability of dehydrogenation versus C–C bond breaking (cracking), we computed the energetics (and barriers) of cracking compared to C–H activation. For the Pt₄Ge cluster, we found no cracking pathways that could compete with C–H activation either thermodynamically or kinetically. The single structure, the result of cracking ethylene, that might compete is shown in Figure S19; however, it is both thermodynamically more uphill than any C–H breaking endpoints and has a higher barrier (1.42 eV) than any of the LM' ethylene dehydrogenation barriers.

The next question posed by the experiments is how Pt₄Ge/alumina retains its high-temperature ethylene binding sites after 21 TPDs, even though the C 1s XPS and ISS results indicated significant carbon deposition. The DFT results indicate that once dehydrogenation has gone beyond ethylene, it should proceed to completion, depositing a pair of C atoms. To test this, we performed global optimization of Pt₄GeC₂/Al₂O₃ (Figure S12), which revealed two pairs of structures. The isomers labeled Split1 and Split2 have similar structures with no CC bond, oriented differently on the support, and the Intact1 and Intact2 isomers have similar structures with a C₂ unit bridging between Pt atoms across the center of the cluster. Intact1 and Intact2 are recognizable as relatives of LM' with an embedded C₂ unit. Since these would form by dehydrogenation of acetylene, the route to forming the intact isomers is clear, but an obvious question is whether the barrier to C–C bond scission is large enough to prevent formation of the split isomers. The computed barrier to C–C bond scission in Pt₄GeC₂ is 1.33 eV, which should inhibit split isomer

formation. Furthermore, the presence of adsorbates (ethane, ethylene, and acetylene) stabilizes the structures with the intact C₂ unit relative to those with the split C₂, making the Intact1 structure the GM. Hence, under reaction conditions, where the clusters are saturated, DFT suggests that the Intact1 structure (also shown in Figure 6A) should be thermodynamically and kinetically favored. Furthermore, we note that the two intact isomers of Figure S12 have near identical reactivities with respect to ethane, ethylene, and acetylene. Finally, note that all these structures have carbon bound such that it does not physically block Pt sites, consistent with ISS observation of minimal Pt attenuation.

The presence of C₂ does, however, alter the electronic structure of the cluster. Generally, we see the C atoms adopting a negative charge when bound only to Pt atoms (Figure S12), though in the case of one isomer, we see that as the C binds to an oxygen in the Al₂O₃ support, it adopts a high positive charge, as might be expected. For the active structures, with the intact C₂ unit, we see that it acts as an oxidant (due to low-lying π states), adopting a net negative charge of either -0.29lel or -0.42lel on the lower energy and higher energy structures, respectively. The Ge in each isomer becomes more positively charged at either $+0.85\text{lel}$ or $+0.80\text{lel}$. Despite their structural similarity, there are subtle differences in the charge distribution of the isomers of the active motif (see Bader charges in Figure S12A). Ultimately, however, each isomer has one Pt atom which remains the active site, which has the same charge (-0.33lel) on each structure. The overall charge on the Pt₄ moiety remains negative, decreased slightly from the values typical for Pt₄Ge isomers but is still higher than that for Pt₄/alumina (Figures 2A and 6A). The interaction of C₂ with Pt₄Ge is strikingly different from its interaction with Pt₄, as shown in Figure S12.

To investigate the electronic structure differences between the Pt₄C₂ and Pt₄GeC₂ clusters in more detail, we performed COHP local bonding analysis for the C–C bonds in Pt₄C₂ and Pt₄GeC₂ (Figure S13). The main feature of these plots is the sharp stabilizing peak which lies above the Fermi level in Pt₄C₂ but immediately below it in Pt₄GeC₂. Combined with the evidence of Ge–C charge transfer, this indicates that the effect of adding Ge is to strengthen the C–C π -bonding in the partially coked cluster.

While Pt₄C₂ and Pt₄GeC₂ are structurally similar, have similar total number of electron transfers from the support, and feature the partially negatively charged C₂ unit, they differ in the source of electron transfer to C₂: in Pt₄GeC₂, C₂ receives electrons largely from Ge, leaving Pt still quite anionic. In Pt₄C₂, C₂ draws electrons from Pt, leaving it closer to the charge neutral state. Thus, it appears that in Pt₄Ge/alumina, Ge and C₂ are in a synergistic electronic relationship that preserves the net negative charge on the Pt₄ moiety. Hence, Pt sites are neither blocked nor significantly changed electronically in Pt₄GeC₂/alumina as compared to Pt₄Ge, and therefore, it is not surprising that Pt₄GeC₂ retains the strong C₂D₄ binding properties seen in the TPD. Hence, we expect the reactivity of the Pt sites in Pt₄GeC₂/alumina to be minimally affected by coking and remain comparable to that of Pt₄Ge/alumina.

The important remaining questions are whether Pt₄GeC₂/alumina is still active for ethane-to-ethylene dehydrogenation and whether it is selective against additional carbon deposition, thereby resisting deactivation. Ethane sticks too weakly to any of these samples to allow the ethane-to-ethylene conversion

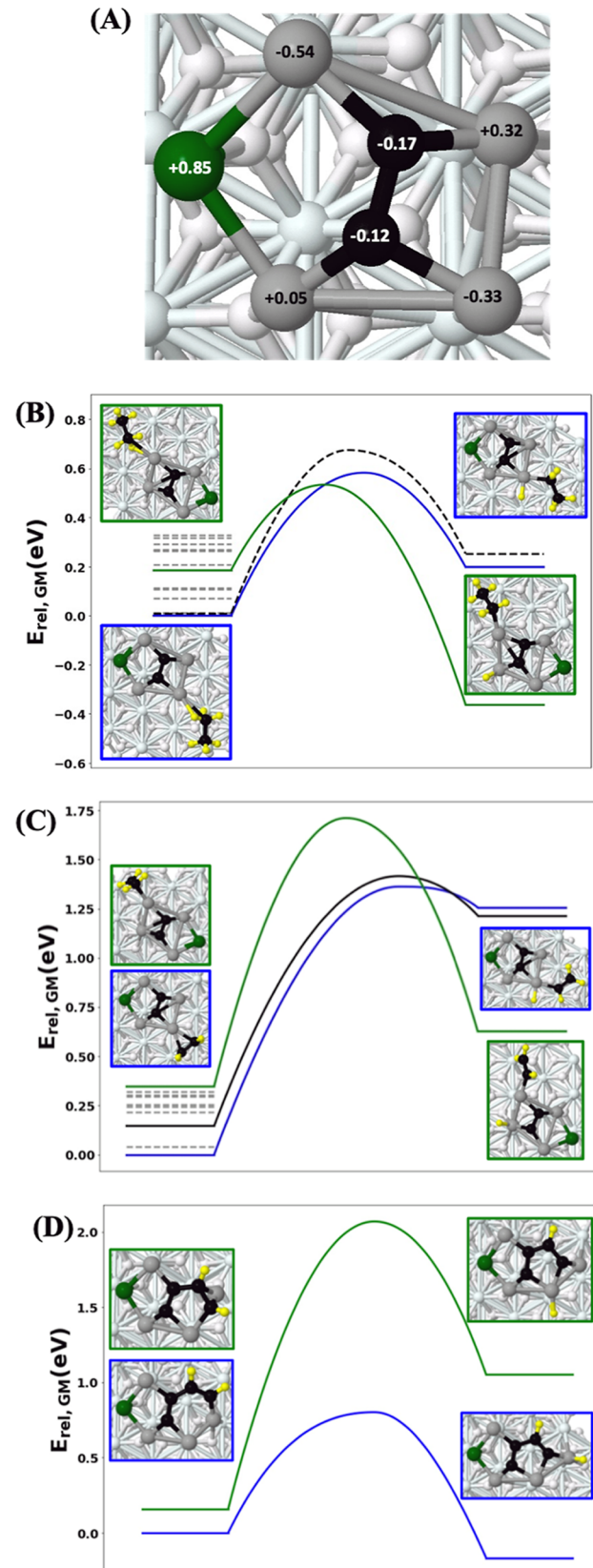


Figure 6. Representative ethane, ethylene, and acetylene C–H activation barriers on Pt₄GeC₂, the steady-state catalyst. (A) One dehydrogenation-active Pt₄GeC₂ isomer motif and representative C–H activation barriers for (B) ethane, (C) ethylene, and (D) acetylene, with certain key structures inset.

process to be studied under our surface science conditions. Therefore, ethane dehydrogenation on Pt_4GeC_2 is addressed by DFT in Figure 6B. Binding of ethane and ethylene on the Pt_4GeC_2 clusters in various geometries was sampled (Figures S14 and S16) and then the barriers for C–H dissociation calculated (Figures S15, S17). Again, adsorbates stabilize the isomers with the intact C_2 motif, which are active for ethane dehydrogenation, with lower C–H activation barriers than desorption energies. This suggests that Pt_4GeC_2 should still be active for ethane to ethylene dehydrogenation. We performed the same analysis of the second C–H activation for the low-barrier C–H activation and found that while the second barrier is slightly higher than the first one, this should not prevent ethylene formation (Figure S6). In contrast, lowest energy Pt_4GeC_2 structure with a split C_2 unit (which we believe is inaccessible) did not chemisorb ethane. To be stable with respect to further carbon deposition, it is necessary that the resulting ethylene desorb instead of dehydrogenating further. For ethylene on $\text{Pt}_4\text{GeC}_2/\text{alumina}$ (Figures S16, S17 and 6C), some configurations were calculated to have highly endothermic (>1.2 eV) dehydrogenation, and in others, the activation barriers were high (>2 eV). Some structures showed the possibility for dehydrogenation of ethylene, with barriers between 1.3 and 1.5 eV to access structures that are not highly endothermic; however, we note that these barriers are higher than those for the dehydrogenation of ethylene on the Pt_4Ge cluster, indicating that the Pt_4GeC_2 cluster is even more selective against ethylene dehydrogenation to form coke precursors than the initial Pt_4Ge catalyst. Acetylene dehydrogenation by Pt_4GeC_2 (Figures 6D, S18) is possible, however, due to the increased selectivity toward ethylene desorption, we consider the catalyst to remain an active catalyst with self-limiting coking. We note that the adsorption energies of acetylene to the cluster are quite high, (around ~3 eV), so we may consider acetylene to act as coke itself, either dehydrogenated or not. This aligns with the experiment, where no acetylene desorption is observed during TPD (Figure S11).

In order to assess possible coke formation via cracking on Pt_4GeC_2 , we also computed the energetics of the C–C bond scission on relevant intermediates. A few of the pathways found are thermodynamically viable, however the kinetics render them unlikely compared to either C–H activation or desorption (Figure S19), with the exception of acetylene cracking, where the barrier is ~0.3 eV higher than the lowest barrier for C–H activation.

Ultimately, however, DFT calculations suggest that while coke formation on the Pt_4Ge system is not avoided, the cluster nonetheless retains its active and selective nature toward alkane dehydrogenation. Thus, the conclusion is that selectively coked $\text{Pt}_4\text{GeC}_2/\text{alumina}$, generated under reaction conditions by a self-limiting coking process, is the actual stable, active, and selective catalytic species for alkane-to-alkene dehydrogenation.

It is interesting to compare the behavior of the Pt_4Ge system to Pt_nB_x and Pt_nSn_x , both of which were studied by similar methods.^{13,16,24} For boron, saturated diborane exposures were used to borate size-selected $\text{Pt}_n/\text{alumina}$, and it was found that ethylene exclusively desorbed intact from the borated catalysts, that is, carbon deposition was suppressed. Unfortunately, however, the high-temperature/strong ethylene binding sites were also completely blocked by boration, suggesting that coking was suppressed only because the ethylene all desorbed

before the dehydrogenation onset temperature was reached.^{16,24} Because these strong binding sites are important for ethane-to-ethylene conversion, boration would, therefore, likely suppress this chemistry. In the case of Sn, a SnCl_4/H_2 treatment, similar to that used for Ge addition, was used to modify Pt_n clusters deposited on both alumina¹³ and silica^{14,25} supports. The treatment yielded alloyed clusters with stoichiometries close to 1:1, for example, Pt_4Sn_3 , when modifying Pt_4 . The Pt_nSn_x clusters on either silica or alumina support were found to almost completely suppress ethylene dehydrogenation, in this case retaining some high-temperature/strong ethylene binding sites, desirable for promoting ethane-to-ethylene conversion. The limitation for Sn alloying was that it resulted in a substantial reduction in the number of such sites compared to Pt_n (or Pt_nGe) which would tend to suppress ethane-to-ethylene activity. The advantage of Ge alloying is that small Ge/Pt ratios are sufficient to strongly modify the cluster electronic and catalytic properties and allow the unique self-limiting coking effect. Another point of comparison is with a recent report from Zheng et al. where selective CO poisoning was used to enhance catalytic hydrogenation reactions on alumina- and titania-supported Pd clusters.²⁶

CONCLUSIONS

In summary, from the TPD, XPS, and DFT results, we found that $\text{Pt}_4\text{Ge}/\text{alumina}$ promotes intact desorption of ethylene in ethane dehydrogenation, largely, but not completely preventing carbon deposition. There is one minority isomer of $\text{Pt}_4\text{Ge}/\text{alumina}$ (LM2, or LM') that acts as a gateway to carbon deposition on $\text{Pt}_4\text{Ge}/\text{alumina}$, gradually resulting in all Pt_4Ge clusters becoming coked. However, contrary to expectations, coking is not detrimental to catalytic activity and instead preserves the desired catalytic properties while enhancing cluster catalyst stability. The coking is self-limiting: once $\text{Pt}_4\text{GeC}_2/\text{alumina}$ forms, it decreases further deposition of carbon by ethylene dehydrogenation through increased C–H activation barriers, eventually reaching a steady-state catalyst where no further changes in the ethylene binding sites or D_2 desorption are observed experimentally. Furthermore, $\text{Pt}_4\text{GeC}_2/\text{alumina}$ still binds ethane strongly, with low activation barriers for ethane-to-ethylene conversion. Thus, the self-limiting coking of Pt_4Ge improves the selectivity of the catalyst without degrading the activity. The Ge atom in the cluster interacts with the carbon in the coked cluster, stabilizing the cluster, and preventing deactivation of the cluster via either physical blocking of sites or dramatic change in electronic structure. This moderates the tendency of the cluster to coke, enabling the self-limiting behavior. The synergy between alloying and selective coking could be a way forward in creating ultra-stable sub-nano cluster catalysts for other reactions, solving the main limiting factor hampering widespread use of sub-nano clusters in catalysis.

METHODS

Instrument Design. Past publications have detailed the instrument design and protocols used in this study.^{13,14,16} In brief, Pt_n^+ cluster ions were produced via laser ablation of a Pt target, collected by a series of quadrupole ion guides, mass selected by a quadrupole mass filter, and then guided into the UHV system, where they were deposited on the catalyst support. The support consisted of a thin alumina film grown

on a Ta(110) single crystal, which was mounted via heater wires to a cryostat allowing temperature control in the 120–1000 K range. For cleaning, the sample could be heated by electron bombardment; from behind the cryostat, a filament allowed bombardment of electrons to the single crystal that could heat the crystal to over 2100 K. At that temperature, the alumina film and any deposited clusters desorb, and the sample was found to be clean by XPS.

Alumina Film Growth. A fresh alumina film was grown on the clean Ta(110) single crystal before each experiment, by evaporating Al in 5×10^{-6} Torr of O₂ at sample temperature of 970 K. These growth conditions produce alumina with a distorted hexagonal lattice that resembles both γ -alumina (111) or α -alumina (0001).^{27,28} Film thickness was monitored by XPS and was in the 4–6 nm range, which we previously found to give chemistry independent of film thickness.²⁹

Pt₄/Alumina Sample Preparation. Pt_n⁺ clusters of the desired size, Pt₄ in this case, were deposited on the alumina film with deposition energy of ~1 eV/atom and coverage equivalent to ~0.1 ML, corresponding to 1.5×10^{14} Pt atoms/cm². Just prior to deposition, the sample was flashed to 750 K to desorb any adventitious adsorbates and then cluster deposition was carried out as the sample cooled, starting at 300 K.

Pt₄Ge/Alumina Sample Preparation. The approach used to prepare alumina-supported Pt_nGe_m clusters was similar to that used in previous studies of Pt_nSn_m/alumina and Pt_nSn_m/SiO₂.^{13,25} In essence, the Pt clusters were used as seeds to obtain selective, self-limiting deposition by exposing the Pt₄/alumina sample to a 60 L dose of GeCl₄ vapor, then to 6000 L of H₂. The GeCl₄ preferentially binds to the Pt_n clusters, and the number of molecules that bind depends on the size of the cluster. When exposed to H₂, Cl reacts and desorbs as HCl, which can be detected mass spectrometrically. The final stage in the preparation was to heat the samples to 750 K to desorb any remaining Cl atoms (as HCl) as well as to remove excess H atoms. The samples were characterized by XPS. The Pt_n clusters were found to “seed” preferential Ge deposition on the clusters, resulting in one Ge atom for every Pt₄ cluster deposited as discussed above. Note that if larger GeCl₄ exposures are used, the amount of Ge deposited does not change. Thus, Ge addition to the clusters is limited by the number of GeCl₄ precursor molecules than can be adsorbed *per* cluster, in this case, one GeCl₄/Pt₄.

Some non-specific Ge deposition at defects in the alumina support film also occurs (as discussed in *Supporting Information*, page S10–S11), but ethylene TPD indicates that these support-bound Ge atoms have little effect on the chemistry of Pt₄ deposited on the Ge-treated alumina. To show this, 0.1 ML Pt₄ clusters were deposited onto alumina supports that had been pre-treated with Ge, using the same protocol used in Ge addition to the clusters (60 L of GeCl₄, 6000 L of H₂). C₂D₄ TPD on these samples gave results very similar to those for Pt₄ deposited on Ge-free alumina. Large dehydrogenation signals implying coking are seen, along with rapid deactivation in repeated TPD cycles; that is, support-bound Ge does not suppress coking and sintering (see *Supporting Information*, Figures S20, S21). As shown in Figure 3, Ge deposited on the clusters has very different results, strongly suppressing coking and stabilizing the clusters.

XPS Quantification. XPS was used to characterize the ratio of Ge to Pt present in the samples and to measure carbon deposition. Samples were analyzed via Al K α XPS and the raw

intensities were corrected to account for slight day-to-day changes in spectrometer sensitivity and X-ray intensity using the Al 2s intensities from the alumina support (details in *Supporting Information*).

TPD Experimental Procedures. TPD was used to investigate C₂D₄ desorption and dehydrogenation/carbon deposition chemistry on the samples. To start each TPD cycle, the samples were held at 150 K and exposed to a 10 L dose of C₂D₄, which is sufficient to saturate all binding sites that are stable at 150 K. The sample was then heated at 3 K *per* second to 750 K while monitoring desorption of species of interest (principally C₂D₄ and D₂) using a differentially pumped mass spectrometer that views the sample through a 2.5 mm aperture on a skimmer cone, positioned ~0.5 mm from the sample surface. The relationship between numbers of molecules desorbing from the sample and numbers of ions detected by the mass spectrometer was determined using a procedure described elsewhere,¹³ calibrated by leaking C₂D₄ or D₂ into the main UHV chamber at measured pressures to create well defined fluxes into the mass spectrometer.

C₂D₄ was used to minimize interference from mass spectrometer background from CO and H₂ which are always present in UHV chambers. For C₂H₄, the intact desorption signal would have interference from CO (both mass 28) and the dehydrogenation signal would have background from H₂. For C₂D₄, detection of possible C₂D₂ product has interference from CO, and experiments were also done with C₂H₄, to verify absence of C₂H₂ desorption. There were no obvious deuteration effects on the ethylene desorption temperature dependence.

Computational Methods. Global optimization of the Pt₄Ge/alumina structures was performed with plane-wave DFT using the Vienna Ab-initio Simulation Package (VASP)^{30–32} with projector augmented wave potentials,³³ using the PBE functional.³⁴ The kinetic energy cutoff for the plane wave basis sets was chosen as 400.0 eV, and Gaussian smearing with a width (σ) of 0.1 eV was used. The convergence criteria for electronic minimization and geometry optimization were 10^{-6} eV and 0.01 eV/Å, respectively. The D3 dispersion correction was used.³⁵ The model substrate used was an α -alumina (0001) surface with cell parameters of $a = 4.807$ Å and $c = 13.126$ Å, previously found²⁰ to best match the experimental support. The lower layers of the slab were kept fixed during global optimization and subsequent adsorbate binding calculations. Only Γ -point sampling was used due to the larger supercell used in the study.

Our initial Pt₄Ge structure geometries were obtained using our in-house code PGOPT,³⁶ which uses a bond-length distribution algorithm in order to generate structures that are faster to optimize and less likely to result in errors during optimization. Once ~200 Pt₄Ge structures had been generated, we took the thermally accessible structures within a cutoff of 0.4 eV and generated a number of rough binding modes of C₂H₆, C₂H₄, and C₂H₂ using PGOPT, which we later refined with VASP local optimizations to obtain the final binding modes. The final ensemble of thermally accessible catalyst states was computed for the initial cluster structures and recomputed for every intermediate on the reaction profile, by weighting the optimized structures by the Boltzmann probability to be occupied at 700 K, based on DFT electronic energies.

The Pt₄GeC₂ structures were generated from the thermally accessible acetylene binding modes to Pt₄Ge by removing the

hydrogens and then optimizing the resulting structures with DFT. Bader charge analysis^{37–40} was performed to obtain the partial atomic charges. C–H activation barriers for low-lying and important binding modes were calculated using the climbing-image nudged elastic band method³⁹ and optimized until the force on all images was less than 0.02 eV/Å. For ethylene and acetylene, multiple non-equivalent C–H bond breaking events were attempted, focusing on the hydrogens closest to Pt atoms. For ethane, only the elongated activated C–H bonds were broken. Adsorption energies of ethane, ethylene, and acetylene to the Pt₄GeC₂ clusters were calculated with the equation $E_{\text{ads}} = E_{\text{clust+ads}} - E_{\text{clust}} - E_{\text{gas}}$, using the bare supported cluster which best matched the cluster core of the adsorbate-bound structure.

Local bonding analysis was performed using the LOBSTER program, version 4.1.0.^{41,42} The PBEvaspfit basis was used with 3s3p basis functions for Al, 2s2p for O and C, 5p5d6s for Pt, and 4s4p for Ge. All projections were converged with a charge spilling of less than 1.2%.

■ ASSOCIATED CONTENT

Supporting Information

The Supporting Information is available free of charge at <https://pubs.acs.org/doi/10.1021/acscatal.2c05634>.

TEM images of Pt₄ clusters, TPD and XPS quantification, sampling protocol, full Pt₄/alumina and Pt₄Ge/alumina structures, binding modes and barriers, COHP analysis, S/TEM images, TPD results, and desorbing molecule numbers Data behind all figures In the paper will be uploaded to a publicly available archive with link provided at the time of publication. Correspondence and requests for materials should be addressed to A.N.A. and S.L.A. ([PDF](#))

■ AUTHOR INFORMATION

Corresponding Authors

Anastassia N. Alexandrova — Department of Chemistry and Biochemistry, University of California Los Angeles, Los Angeles, California 90095, United States;  orcid.org/0000-0002-3003-1911; Email: ana@chem.ucla.edu

Scott L. Anderson — Department of Chemistry, University of Utah, Salt Lake City, Utah 84112, United States;  orcid.org/0000-0001-9985-8178; Email: anderson@chem.utah.edu

Authors

Patricia Poths — Department of Chemistry and Biochemistry, University of California Los Angeles, Los Angeles, California 90095, United States;  orcid.org/0000-0003-4193-526X

Guangjing Li — Department of Chemistry, University of Utah, Salt Lake City, Utah 84112, United States

Tsugunosuke Masubuchi — Department of Chemistry, University of Utah, Salt Lake City, Utah 84112, United States;  orcid.org/0000-0001-9381-0077

Harry W. T. Morgan — Department of Chemistry and Biochemistry, University of California Los Angeles, Los Angeles, California 90095, United States;  orcid.org/0000-0001-9647-8807

Zisheng Zhang — Department of Chemistry and Biochemistry, University of California Los Angeles, Los Angeles, California 90095, United States

Complete contact information is available at:

<https://pubs.acs.org/10.1021/acscatal.2c05634>

Author Contributions

P.P. and G.L. made equal contributions. A.N.A. and S.L.A. were the senior authors. A.N.A. and S.L.A. conceived and supervised the research, reviewed, and edited the paper. G.L. and P.P. wrote the original draft and developed the methodology. G.L. performed the experimental work. P.P. conducted all DFT calculations. T.M. assisted in obtaining the initial experimental conditions and conducted TEM experiments.

Funding

The funding is from Air Force Office of Scientific Research grant AFOSR FA9550-19-1-0261.

Notes

The authors declare no competing financial interest.

■ ACKNOWLEDGMENTS

We thank Marc Malek and Autumn Fuchs for their assistance with some experiments and Brian Roy Van Devener for collecting the TEM images.

■ REFERENCES

- (1) Oliver-Meseguer, J.; Cabrero-Antonino, J. R.; Domínguez, I.; Leyva-Pérez, A.; Corma, A. *Science* **2012**, *338*, 1452–1455.
- (2) Zandkarimi, B.; Alexandrova, A. N. *J. Phys. Chem. Lett.* **2019**, *10*, 460–467.
- (3) Joo, S. H.; Park, J. Y.; Tsung, C.-K.; Yamada, Y.; Yang, P.; Somorjai, G. A. *Nat. Mater.* **2008**, *8*, 126.
- (4) Bhasin, M. M.; McCain, J. H.; Vora, B. V.; Imai, T.; Pujado, P. R. *Appl. Catal., A* **2001**, *221*, 397–419.
- (5) Nie, L.; Meng, A.; Yu, J.; Jaroniec, M. *Sci. Rep.* **2013**, *3*, 3215.
- (6) Yang, D.; Fu, S.; Huang, S.; Deng, W.; Wang, Y.; Guo, L.; Ishihara, T. *Microporous Mesoporous Mater.* **2020**, *296*, 109802.
- (7) Musselwhite, N.; Na, K.; Sabyrov, K.; Alayoglu, S.; Somorjai, G. A. *J. Am. Chem. Soc.* **2015**, *137*, 10231–10237.
- (8) Lu, J.; Elam, J. W.; Stair, P. C. *Acc. Chem. Res.* **2013**, *46*, 1806–1815.
- (9) Lu, J. L.; Fu, B. S.; Kung, M. C.; Xiao, G. M.; Elam, J. W.; Kung, H. H.; Stair, P. C. *Science* **2012**, *335*, 1205–1208.
- (10) Gorey, T. J.; Dai, Y.; Anderson, S. L.; Lee, S.; Lee, S.; Seifert, S.; Winans, R. E. *Surf. Sci.* **2020**, *691*, 121485.
- (11) Pham, H. N.; Sattler, J. J.; Weckhuysen, B. M.; Datye, A. K. *ACS Catal.* **2016**, *6*, 2257–2264.
- (12) Iglesias-Juez, A.; Beale, A. M.; Maaiken, K.; Weng, T. C.; Glatzel, P.; Weckhuysen, B. M. *J. Catal.* **2010**, *276*, 268–279.
- (13) Li, G.; Zandkarimi, B.; Cass, A. C.; Gorey, T. J.; Allen, B. J.; Alexandrova, A. N.; Anderson, S. L. *J. Chem. Phys.* **2020**, *152*, 024702.
- (14) Gorey, T. J.; Zandkarimi, B.; Li, G.; Baxter, E. T.; Alexandrova, A. N.; Anderson, S. L. *ACS Catal.* **2020**, *10*, 4543–4558.
- (15) Zandkarimi, B.; Gorey, T. J.; Li, G.; Munarriz, J.; Anderson, S. L.; Alexandrova, A. N. *Chem. Mater.* **2020**, *32*, 8595–8605.
- (16) Ha, M.-A.; Baxter, E. T.; Cass, A. C.; Anderson, S. L.; Alexandrova, A. N. *J. Am. Chem. Soc.* **2017**, *139*, 11568–11575.
- (17) Jimenez-Izal, E.; Liu, J.-Y.; Alexandrova, A. J. *Catal.* **2019**, *374*, 93–100.
- (18) Mariscal, R.; Fierro, J. L.; Yori, J. C.; Parera, J. M.; Grau, J. M. *Appl. Catal., A* **2007**, *327*, 123–131.
- (19) Ballarini, A. D.; de Miguel, S.; Castro, A.; Scelza, O. *Catal. Ind.* **2013**, *5*, 283–296.
- (20) Baxter, E. T.; Ha, M.-A.; Cass, A. C.; Alexandrova, A. N.; Anderson, S. L. *ACS Catal.* **2017**, *7*, 3322–3335.
- (21) Redhead, P. A. *Vacuum* **1962**, *12*, 203–211.
- (22) Yeh, J. J.; Lindau, I. *At. Data Nucl. Data Tables* **1985**, *32*, 1–155.

- (23) Dai, Y.; Gorey, T. J.; Anderson, S. L.; Lee, S.; Lee, S.; Seifert, S.; Winans, R. E. *J. Phys. Chem. C* **2017**, *121*, 361–374.
- (24) Baxter, E. T.; Ha, M.-A.; Cass, A. C.; Zhai, H.; Alexandrova, A. N.; Anderson, S. L. *J. Phys. Chem. C* **2018**, *122*, 1631–1644.
- (25) Gorey, T. J.; Zandkarimi, B.; Li, G.; Baxter, E. T.; Alexandrova, A. N.; Anderson, S. L. *J. Phys. Chem. C* **2019**, *123*, 16194–16209.
- (26) Qin, R.; Wang, P.; Liu, P.; Mo, S.; Gong, Y.; Ren, L.; Xu, C.; Liu, K.; Gu, L.; Fu, G. *Research* **2020**, *2020*, 1–9.
- (27) Madey, T. E. *Chemisorption and Reactivity on Supported Clusters and Thin Films*; Lambert, R. M., Pacchioni, G., Eds.; Kluwer Academic Publishers: Netherlands, 1997; Vol. 331, pp 105–116.
- (28) Chen, P. J.; Goodman, D. W. *Surf. Sci.* **1994**, *312*, L767–L773.
- (29) Kane, M. D.; Roberts, F. S.; Anderson, S. L. *J. Phys. Chem. C* **2015**, *119*, 1359–1375.
- (30) Kresse, G.; Hafner, J. *Phys. Rev. B: Condens. Matter Mater. Phys.* **1993**, *47*, 558.
- (31) Kresse, G.; Furthmüller, J. *Phys. Rev. B: Condens. Matter Mater. Phys.* **1996**, *54*, 11169.
- (32) Kresse, G.; Furthmüller, J. *Comput. Mater. Sci.* **1996**, *6*, 15–50.
- (33) Kresse, G.; Joubert, D. *Phys. Rev. B: Condens. Matter Mater. Phys.* **1999**, *59*, 1758–1775.
- (34) Perdew, J. P.; Burke, K.; Ernzerhof, M. *Phys. Rev. Lett.* **1996**, *77*, 3865.
- (35) Grimme, S.; Antony, J.; Ehrlich, S.; Krieg, H. *J. Chem. Phys.* **2010**, *132*, 154104.
- (36) Zhai, H.; Alexandrova, A. N. *J. Chem. Theory Comput.* **2016**, *12*, 6213–6226.
- (37) Tang, W.; Sanville, E.; Henkelman, G. *J. Phys.: Condens. Matter* **2009**, *21*, 084204.
- (38) Sanville, E.; Kenny, S. D.; Smith, R.; Henkelman, G. *J. Comput. Chem.* **2007**, *28*, 899–908.
- (39) Henkelman, G.; Uberuaga, B. P.; Jónsson, H. *J. Chem. Phys.* **2000**, *113*, 9901–9904.
- (40) Yu, M.; Trinkle, D. R. *J. Chem. Phys.* **2011**, *134*, 064111.
- (41) Dronskowski, R.; Bloechl, P. E. *J. Phys. Chem.* **1993**, *97*, 8617–8624.
- (42) Maintz, S.; Deringer, V. L.; Tchougréeff, A. L.; Dronskowski, R. *J. Comput. Chem.* **2016**, *37*, 1030–1035.

□ Recommended by ACS

Influence of Brønsted Acid-Site Density on Reaction-Diffusion Phenomena that Govern Propene Oligomerization Rate and Selectivity in MFI Zeolites

Elizabeth E. Bickel, Rajamani Gounder, et al.

JANUARY 05, 2023

ACS CATALYSIS

READ ▶

Influence of Brønsted Acid Site Proximity on Alkane Cracking in MFI Zeolites

Tram N. Pham, Steven Crossley, et al.

JANUARY 09, 2023

ACS CATALYSIS

READ ▶

Kinetic Insights into the Tandem and Simultaneous Mechanisms of Propylene Epoxidation by H₂ and O₂ on Au-Ti Catalysts

Wei Du, Xinggui Zhou, et al.

JANUARY 24, 2023

ACS CATALYSIS

READ ▶

Selective Tandem CO₂-to-C₂₊ Alcohol Conversion at a Single-Crystal Au/Cu Bimetallic Interface

Chenyuan Zhu, Liming Zhang, et al.

FEBRUARY 13, 2023

THE JOURNAL OF PHYSICAL CHEMISTRY C

READ ▶

Get More Suggestions >